

Accelerated Articles**Multispectral Thin Film Biosensing and Quantitative Imaging Using 3D Plasmonic Crystals****Matthew E. Stewart,<sup>†</sup> Jimin Yao,<sup>‡</sup> Joana Maria,<sup>‡</sup> Stephen K. Gray,<sup>§</sup> John A. Rogers,<sup>†,‡</sup> and Ralph G. Nuzzo<sup>\*,†,‡</sup>***Department of Chemistry, University of Illinois at Urbana-Champaign, Urbana, Illinois 61801, Department of Materials Science and Engineering, University of Illinois at Urbana-Champaign, Urbana, Illinois 61801, and Center for Nanoscale Materials, Argonne National Laboratory, Argonne, Illinois 60439*

This work provides plasmonic crystal platforms for quantitative imaging mode biosensing and multispectral immunoassays, establishing and validating both the optical and equilibrium bases for their operation. We investigated the distance-dependent refractive index sensitivity of full 3D plasmonic crystals to thin polymeric films formed using layer by layer (LbL) assembly of polyelectrolytes as a model system. LbL was also used to determine the preferred gold thickness and plasmonic crystal design rules (nanowell diameter and periodicity) for improved thin-film sensitivity, and full 3D finite-difference time-domain (FDTD) calculations were used to quantitatively model and confirm the experimentally observed thin film sensitivities. The integrated multispectral response of the crystals increases approximately linearly with film thickness for values <70 nm, which enables the use of molecular rulers with known thicknesses (such as self-assembled monolayers of alkanethiols on gold) to calibrate these optics for quantitative detection and speciation of surface binding events in a multiplexed imaging format. The utility of these sensors and multispectral analysis for applications in quantitative biosensing was further demonstrated by measuring the equilibrium response curve of an antibody/antigen pair (rabbit antigoat IgG/goat IgG) at increasing antigen concentrations. Fitting the integrated response to a Langmuir isotherm yielded a calculated binding constant on the order of  $\sim 10^7 \text{ M}^{-1}$ , which is in agreement with the affinity constants reported in the literature for anti-IgG/IgG binding pairs and provides intrinsic detection limits of  $\sim 400 \text{ pM}$  for such unamplified assays.

Surface plasmon resonance (SPR) spectroscopy has become a valuable tool for enabling real-time, label-free detection of biomolecular interactions in both singular<sup>1–4</sup> and multiplexed formats.<sup>5–12</sup> This technique exploits the sensitivity of surface plasmons to changes in the refractive index (RI) occurring at a metal (typically gold or silver)–dielectric interface and has found utility in applications ranging from fundamental studies of the thermodynamics and kinetics of biomolecular interactions<sup>13–15</sup> to

\* Corresponding author. Ralph G. Nuzzo, University of Illinois, 600 South Mathews Avenue, Urbana, IL 61801. Phone: 217-244-0809. Fax: 217-244-2278. E-mail: r-nuzzo@illinois.edu.

<sup>†</sup> Department of Chemistry, University of Illinois at Urbana-Champaign.

<sup>‡</sup> Department of Materials Science and Engineering, University of Illinois at Urbana-Champaign.

<sup>§</sup> Argonne National Laboratory.

- (1) Homola, J. *Chem. Rev.* **2008**, *108*, 462–493.
- (2) Solanki, P. R.; Prabhakar, N.; Pandey, M. K.; Malhotra, B. D. *Biomed. Microdevices* **2008**, *10*, 757–767.
- (3) Cheng, F.; Gamble, L. J.; Castner, D. G. *Anal. Chem.* **2008**, *80*, 2564–2573.
- (4) Mazumdar, S. D.; Hartmann, M.; Kaempfer, P.; Keusgen, M. *Biosens. Bioelectron.* **2007**, *22*, 2040–2046.
- (5) Liu, W.; Chen, Y.; Yan, M. *Analyst* **2008**, *133*, 1268–1273.
- (6) Singh, B. K.; Hillier, A. C. *Anal. Chem.* **2007**, *79*, 5124–5132.
- (7) Wang, Z.; Wilkop, T.; Han, J. H.; Dong, Y.; Linman, M. J.; Cheng, Q. *Anal. Chem.* **2008**, *80*, 6397–6404.
- (8) Lockett, M. R.; Weibel, S. C.; Phillips, M. F.; Shortreed, M. R.; Sun, B.; Corn, R. M.; Hamers, R. J.; Cerrina, F.; Smith, L. M. *J. Am. Chem. Soc.* **2008**, *130*, 8611–8613.
- (9) Li, Y.; Lee, H. J.; Corn, R. M. *Anal. Chem.* **2007**, *79*, 1082–1088.
- (10) Corne, C.; Fiche, J.-B.; Gasparutto, D.; Cunin, V.; Suraniti, E.; Buhot, A.; Fuchs, J.; Calemczuk, R.; Livache, T.; Favier, A. *Analyst* **2008**, *133*, 1036–1045.
- (11) Luo, Y.; Yu, F.; Zare, R. N. *Lab Chip* **2008**, *8*, 694–700.
- (12) Ladd, J.; Taylor, A. D.; Piliarik, M.; Homola, J.; Jiang, S. *Anal. Chem.* **2008**, *80*, 4231–4236.
- (13) Helmholtz, H.; Naatz, S.; Lassen, S.; Prange, A. *J. Chromatogr., B: Anal. Technol. Biomed. Life Sci.* **2008**, *871*, 60–66.
- (14) Park, H.; Germini, A.; Sforza, S.; Corradini, R.; Marchelli, R.; Knoll, W. *Biointerphases* **2006**, *1*, 113–122.

medical diagnostics,<sup>1,16–18</sup> environmental monitoring,<sup>1,19,20</sup> and food safety.<sup>21–23</sup>

Propagating surface plasmon polaritons (SPPs) and localized surface plasmon resonances (LSPRs) are two types of SPRs used for sensing.<sup>24</sup> SPPs can be excited by light at a metal–dielectric interface using prism, waveguide, or grating couplers.<sup>1,25</sup> These plasmons propagate along a metal–dielectric interface with an electric field that decays exponentially over hundreds of nanometers into the dielectric.<sup>1,25</sup> LSPRs are nonpropagating resonances that can be directly excited by light on nanostructured metals, such as nanoparticles<sup>26–29</sup> and around nanoholes<sup>30,31</sup> and nanowells<sup>24,32,33</sup> in metal films, and have an associated electric field that decays exponentially from the surface over tens of nanometers.<sup>34,35</sup> The decay lengths of the electric fields associated with SPPs and LSPRs impact the linearity and surface sensitivity of techniques that utilize them for sensing.<sup>35–38</sup>

We recently described two types of plasmonic crystals (quasi-3D and full-3D) formed by soft nanoimprint lithography that enable plasmonic imaging of binding events with micrometer spatial resolution and submonolayer sensitivity in a normal incidence transmission configuration using a common optical microscope

and low-cost charge coupled device (CCD) camera.<sup>32,39,40</sup> This simple collinear transmission configuration is robust and does not require cumbersome optics or alignment to a specific contrast angle, which allows the devices to be easily incorporated into microfluidic systems, well plates, or portable devices. These crystals exhibit complex optical responses and support Bloch-wave SPPs (BW-SPPs, the periodic analog of SPPs), LSPRs, related diffractive effects such as Wood anomalies (WAs),<sup>41–43</sup> and combinations of these resonant and diffractive phenomena.<sup>32,44</sup> Previous work<sup>32,40</sup> studied the multispectral response of the crystals to solutions of increasing RI, which uniformly changes the RI of the dielectric within the evanescent field of the plasmonic modes. These bulk solution RI studies do not reflect the conditions that are encountered during biosensing experiments where RI changes due to biomolecular interactions at the metal–dielectric interface occur within a fraction of the evanescent field (surface versus bulk RI changes).

Electrostatic layer-by-layer (LbL) assembly of polyelectrolytes has been used to form thin films of known thickness and composition on a variety of supports including planar surfaces, microparticles, and nanoporous templates.<sup>45–47</sup> In the present work, LbL assembly of thin polyelectrolyte films<sup>48–50</sup> is used to directly study the surface sensitivity of full 3D plasmonic crystals, which yields useful information for biosensing applications regarding the sensing volume, linearity, and distance-dependent optical response of the crystals. The effects of gold thickness and design rules (nanowell diameter and periodicity) on the sensitivity of these devices are investigated, and the optical response is quantitatively modeled using full 3D finite-difference time-domain (FDTD) calculations. This systematic study reveals that crystals with a 120 nm thick layer of gold exhibit greater surface sensitivity than crystals with thicker or thinner gold films. We also demonstrate that the linear response of the crystals can be used together with molecular rulers, molecular assemblies with known thicknesses such as self-assembled monolayers (SAMs) of alkanethiols on gold,<sup>51–54</sup> to calibrate these systems for quantitative imaging and speciation of surface binding events. Quantitative real-time multispectral biosensing is also demonstrated, where equilibrium

(15) Linman, M. J.; Taylor, J. D.; Yu, H.; Chen, X.; Cheng, Q. *Anal. Chem.* **2008**, *80*, 4007–4013.

(16) Vaisocherova, H.; Homola, J. In *Surface Plasmon Resonance Based Sensors*; Homola, J., Ed.; Springer-Verlag: New York, 2006; Vol. 4, pp 229–247.

(17) Cherif, B.; Roget, A.; Villiers, C. L.; Calemczuk, R.; Leroy, V.; Marche, P. N.; Livache, T.; Villiers, M.-B. *Clin. Chem.* **2006**, *52*, 255–262.

(18) Haes, A. J.; Van Duyne, R. P. *Expert Rev. Mol. Diagn.* **2004**, *4*, 527–537.

(19) Dostalek, J.; Homola, J. In *Surface Plasmon Resonance Based Sensors*; Homola, J., Ed.; Springer-Verlag: New York, 2006; Vol. 4, pp 191–206.

(20) Mauriz, E.; Calle, A.; Manclus, J. J.; Montoya, A.; Lechuga, L. M. *Anal. Bioanal. Chem.* **2007**, *387*, 1449–1458.

(21) McWhirter, A.; Wahlstroem, L. In *Handbook of Surface Plasmon Resonance*; Royal Society of Chemistry: Cambridge, U.K., 2008, pp 333–353.

(22) Ladd, J.; Taylor, A. D.; Homola, J.; Jiang, S. *Sens. Actuators, B* **2008**, *B130*, 129–134.

(23) Llamas, N. M.; Stewart, L.; Fodey, T.; Higgins, H. C.; Velasco, M. L. R.; Botana, L. M.; Elliott, C. T. *Anal. Bioanal. Chem.* **2007**, *389*, 581–587.

(24) Stewart, M. E.; Anderton, C. R.; Thompson, L. B.; Maria, J.; Gray, S. K.; Rogers, J. A.; Nuzzo, R. G. *Chem. Rev.* **2008**, *108*, 494–521.

(25) Homola, J. *Anal. Bioanal. Chem.* **2003**, *377*, 528–539.

(26) Zhao, J.; Das, A.; Schatz, G. C.; Sliagar, S. G.; Van Duyne, R. P. *J. Phys. Chem. C* **2008**, *112*, 13084–13088.

(27) Hu, M.; Chen, J.; Li, Z.-Y.; Au, L.; Hartland, G. V.; Li, X.; Marquez, M.; Xia, Y. *Chem. Soc. Rev.* **2006**, *35*, 1084–1094.

(28) Hu, M.; Novo, C.; Funston, A.; Wang, H.; Staleva, H.; Zou, S.; Mulvaney, P.; Xia, Y.; Hartland, G. V. *J. Mater. Chem.* **2008**, *18*, 1949–1960.

(29) Chan, G. H.; Zhao, J.; Schatz, G. C.; Van Duyne, R. P. *J. Phys. Chem.* **2008**, *112*, 13958–13963.

(30) Ebbesen, T. W.; Lezec, H. J.; Ghaemi, H. F.; Thio, T.; Wolff, P. A. *Nature* **1998**, *391*, 667–669.

(31) Barnes, W. L.; Murray, W. A.; Dintinger, J.; Devaux, E.; Ebbesen, T. W. *Phys. Rev. Lett.* **2004**, *92*, 107401/107401–107401/107404.

(32) Stewart, M. E.; Mack, N. H.; Malyarchuk, V.; Soares, J. A. N. T.; Lee, T.-W.; Gray, S. K.; Nuzzo, R. G.; Rogers, J. A. *Proc. Natl. Acad. Sci. U.S.A.* **2006**, *103*, 17143–17148.

(33) Kelf, T. A.; Sugawara, Y.; Cole, R. M.; Baumberg, J. J.; Abdelsalam, M. E.; Cintra, S.; Mahajan, S.; Russell, A. E.; Bartlett, P. N. *Phys. Rev. B* **2006**, *74*, 245415/245411–245415/245412.

(34) Willets, K. A.; Van Duyne, R. P. *Annu. Rev. Phys. Chem.* **2007**, *58*, 267–297.

(35) Whitney, A. V.; Elam, J. W.; Zou, S.; Zinovev, A. V.; Stair, P. C.; Schatz, G. C.; Van Duyne, R. P. *J. Phys. Chem. B* **2005**, *109*, 20522–20528.

(36) Jung, L. S.; Campbell, C. T.; Chinowsky, T. M.; Mar, M. N.; Yee, S. S. *Langmuir* **1998**, *14*, 5636–5648.

(37) Yonzon, C. R.; Jeoung, E.; Zou, S.; Schatz, G. C.; Mrksich, M.; Van Duyne, R. P. *J. Am. Chem. Soc.* **2004**, *126*, 12669–12676.

(38) Haes, A. J.; Zou, S.; Schatz, G. C.; Van Duyne, R. P. *J. Phys. Chem. B* **2004**, *108*, 109–116.

(39) Malyarchuk, V.; Stewart, M. E.; Nuzzo, R. G.; Rogers, J. A. *Appl. Phys. Lett.* **2007**, *90*, 203113/203111–203113/203113.

(40) Yao, J.; Stewart, M. E.; Maria, J.; Lee, T.-W.; Gray, S. K.; Rogers, J. A.; Nuzzo, R. G. *Angew. Chem., Int. Ed.* **2008**, *47*, 5013–5017.

(41) Sarrazin, M.; Vigneron, J.-P.; Vigoureux, J.-M. *Phys. Rev. B* **2003**, *67*, 085415/085411–085415/085418.

(42) Wood, R. W. *Phil. Mag.* **1902**, *4*, 396–402.

(43) Hessel, A.; Oliner, A. A. *Appl. Opt.* **1965**, *4*, 1275–1297.

(44) Chang, S.-H.; Gray, S. K.; Schatz, G. C. *Opt. Express* **2005**, *13*, 3150–3165.

(45) Lee, D.; Cohen, R. E.; Rubner, M. F. *Langmuir* **2007**, *23*, 123–129.

(46) Decher, G.; Schlenoff, J. B., Eds. *Multilayer Thin Films: Sequential Assembly of Nanocomposite Materials*; Wiley-VCH: Weinheim, Germany, 2003.

(47) Caruso, F., Ed. *Colloids and Colloid Assemblies: Synthesis, Modification, Organization and Utilization of Colloid Particles*; Wiley-VCH: Weinheim, Germany, 2004.

(48) Caruso, F.; Niikura, K.; Furlong, N. D.; Okahata, Y. *Langmuir* **1997**, *13*, 3422–3426.

(49) Schneider, G.; Decher, G. *Langmuir* **2008**, *24*, 1778–1789.

(50) Zhang, X.; Chen, H.; Zhang, H. *Chem. Commun.* **2007**, 1395–1405.

(51) Love, C. J.; Estroff, L. A.; Kriebel, J. K.; Nuzzo, R. G.; Whitesides, G. M. *Chem. Rev.* **2005**, *105*, 1103–1169.

(52) Dubois, L. H.; Zegarski, B. R.; Nuzzo, R. G. *J. Chem. Phys.* **1993**, *98*, 678–688.

(53) Dubois, L. H.; Nuzzo, R. G. *Annu. Rev. Phys. Chem.* **1992**, *43*, 437–463.

(54) Bain, C. D.; Troughton, E. B.; Tao, Y. T.; Evall, J.; Whitesides, G. M.; Nuzzo, R. G. *J. Am. Chem. Soc.* **1989**, *111*, 321–335.

analysis is performed to determine the affinity constant of a model antibody–antigen pair and validate the operating response curve for a nonamplified immunoassay using an integrated response over a broad range of wavelengths. The ability to perform quantitative bioassays in spectroscopic and imaging modes, together with compact form factors, low-cost fabrication procedures, and opportunities for direct integration into microfluidic networks, arrays, or well plates demonstrate several attractive features of these sensing platforms.

## EXPERIMENTAL SECTION

**Chemicals and Materials.** All reagents were used as received without further purification. Manganese(II) chloride tetrahydrate, poly(sodium 4-styrenesulfonate) (PSS, MW = 70 000 g/mol), poly(allylamine hydrochloride) (PAH, MW = 70 000 g/mol), 4,4'-dithiodibutyric acid (DTBA), *N*-hydroxysuccinimide (NHS), *N*-(3-dimethylaminopropyl)-*N*-ethylcarbodiimide hydrochloride (EDC), protein G, antigoat immunoglobulin G (IgG) from rabbit, goat IgG,  $\gamma$ -globulins (bovine), fibrinogen (bovine), albumin (bovine), and myoglobin (human) were purchased from Sigma-Aldrich. Polydimethylsiloxane (PDMS, Sylgard 184) was obtained from Ellsworth Adhesives and prepared according to the manufacturer's directions. Norland Optical Adhesive 73 (NOA) was obtained from Norland Products. Phosphate buffered saline (PBS) was obtained from HyClone (Thermo Scientific) and used to prepare all protein solutions. Deionized (DI) (18 m $\Omega$ ), ultrapure water from a Millipore Milli-Q Academic A-10 system, was used to prepare all polyelectrolyte solutions and was used in all rinsing steps.

**Fabrication of 3D Plasmonic Crystals.** Square arrays of cylindrical nanowells were molded into the surface of a UV curable polymer (NOA) using a soft nanoimprint technique<sup>55</sup> that yields large-area, spatially uniform arrays.<sup>32,40</sup> Briefly, a composite PDMS stamp was used to emboss NOA drop-coated on a glass slide. The NOA was cured by exposure to UV light passed through the PDMS stamp for 3 min. After the PDMS was separated from the NOA, tin oxide (10 nm) and gold films (various thicknesses) were deposited on the embossed NOA by sputter deposition in 5 mTorr argon (AJA International).

**Multilayer Film Preparation and Characterization.** Carboxyl terminated SAMs were formed on the surface of the gold plasmonic crystals by incubating the crystals in ethanolic solutions of DTBA (33 mM) for 24 h. After incubation, the crystals were rinsed thoroughly with ethanol and dried under a stream of nitrogen. Polyelectrolyte layers were formed on the crystals using a previously reported LbL protocol<sup>148</sup> where PAH and PSS are alternately adsorbed on the carboxyl terminated surfaces. Briefly, the crystals were immersed in a PAH polycation solution (3 mg/mL, pH = 8.0) for 5 min, rinsed with water, and then immersed in a PSS polyanion solution (3 mg/mL, pH = 2.0, 1 M MnCl<sub>2</sub>) for 1.5 min and rinsed with water. The polycation and polyanion immersion steps were repeated sequentially until a desired film thickness was achieved. LbL assembly of polyelectrolytes was performed on crystals with no gold film by depositing a thin film of SiO<sub>2</sub> to provide the requisite surface charge for electrostatic adsorption of the initial polycation PAH layer.

**Transmission Measurements.** The optical response of the crystals to increasing thickness of the polyelectrolyte multilayer

was characterized by collecting normal incidence transmission spectra (Varian, Cary 5G spectrophotometer) of the crystals during the assembly process. *In situ* (in water) measurements were performed by placing a crystal in a flow cell and alternately passing solutions of PAH and PSS over the crystal. Unbound polyelectrolyte was removed from the flow cell between each PAH and PSS injection by thoroughly rinsing the flow cell with water. The water rinse also provided a common solution with a known bulk RI for measuring the spectral changes induced by the adsorption of each layer onto the surface of the crystal, where the spectrum of the crystal after each layer was referenced to the initial spectrum of the crystal in water with no layers. *Ex situ* (in air) measurements were performed by collecting spectra of the crystals in air after each polyelectrolyte layer was formed. For these experiments, the crystals were thoroughly rinsed with water and gently dried under a stream of nitrogen prior to the measurement of each layer and before the addition of the next layer. The spectra were compiled and analyzed in Matlab, and plots of the changes in transmission as a function of film thickness were generated using the 2D plot function after noise in the spectra was reduced using a moving average.

**Thin Film Thickness Measurements.** The thicknesses of the polyelectrolyte multilayers were determined in separate experiments. To this end, thin films of tin oxide (10 nm) and gold (50 nm) were formed on glass microscope slides by sputter deposition, and the gold surfaces were modified using the same SAM and multilayer assembly processes (*ex situ* and *in situ*) described above. The *ex situ* thickness of the multilayers in air was determined by ellipsometry (Gaertner, L116C), and the *in situ* thickness of the multilayers in water was determined using a home-built SPR spectrometer and a previously reported method for quantitative analysis of thin films by SPR.<sup>36</sup>

**Finite-Difference Time-Domain (FDTD) Calculations.** Full 3D FDTD calculations were used to model the normal incidence transmission spectra of crystals with different design rules and polyelectrolyte film thicknesses.<sup>44,56</sup> Such calculations represent numerically rigorous solutions of Maxwell's equations that allow one to predict the optical response of the 3D plasmonic crystals. The calculations were performed using a 190  $\times$  190  $\times$  750 grid in *x,y,z* space with a grid resolution of 4 nm. The various layers are taken to be parallel to the *x-y* plane. Appropriate periodic boundary conditions consistent with an infinite square nanowell array in the *x-y* plane are assumed and perfectly matched absorbing layers in the lower and upper parts of *z* are applied to remove light as it is scattered outside the grid. A schematic diagram of the unit cell used in the calculations can be found in the Supporting Information (Figure S1). A time-windowed plane wave was launched from the polymer side, and the zero-order transmission spectrum was calculated above the gold on the air side. The wavelength dependence of the relative dielectric constant of gold was described by a Drude plus two-pole Lorentzian model,<sup>57</sup> with parameters fit to match experimental data for gold over the range of 350–1500 nm.<sup>58</sup> The dielectric constants of

(56) Taflove, A.; Hagness, S. C. *Computational Electrodynamics: The Finite-Difference Time-Domain Method*, 3rd ed.; Artech House Publishers: Norwood, MA, 2005.

(57) Gray, S. K.; Kupka, T. *Phys. Rev. B* **2003**, *68*, 045415/045411–045415/045411.

(58) Lee, T.-W.; Gray, S. K. *Opt. Express* **2005**, *13*, 9652–9659.

(55) Malyarchuk, V.; Hua, F.; Mack, N. H.; Velasquez, V. T.; White, J. O.; Nuzzo, R. G.; Rogers, J. A. *Opt. Express* **2005**, *13*, 5669–5675.

NOA,<sup>59</sup> the polyelectrolyte multilayer,<sup>60,61</sup> and air were taken to be 2.4, 2.2, and 1.0, respectively. Note that although the polyelectrolyte layer is composed of alternating PAH and PSS layers, this multilayer film can be reasonably modeled as a uniform medium with a single effective dielectric constant.

**Microfluidic Patterning of Plasmonic Crystals.** A PDMS microfluidic device with a series of three parallel channels each  $\sim 60 \mu\text{m}$  wide was formed by casting and curing PDMS against a topographically patterned master consisting of photoresist on a silicon wafer. The PDMS device was placed in conformal contact with a plasmonic crystal and each channel was filled with a 0.1 mg/mL solution of either fibrinogen,  $\gamma$ -globulins, or myoglobin in PBS using the channel outgas technique.<sup>62</sup> After incubation for 1 h, the channels were rinsed with PBS and the microfluidic device was removed from the plasmonic crystal. The crystal was then rinsed with water and dried under a stream of nitrogen.

**Two-Dimensional Spatial Imaging of Protein Patterns.** Transmission mode images of proteins microfluidically patterned on the surface of a plasmonic crystal were collected using an Axiovert 200 M inverted research-grade microscope (Carl Zeiss). The sample was illuminated with white light at normal incidence, and the zero-order transmitted light was collected with a 10 $\times$  objective and projected onto a Cascade 512B back-illuminated, frame-transfer EMCCD camera (Roper Scientific). This 16-bit camera operates at 245 K and has a 512  $\times$  512 array of imaging pixels, each of which is 16  $\mu\text{m}$   $\times$  16  $\mu\text{m}$ . Raw images had smooth variations in brightness where the periphery of each image was less illuminated than the center. This uneven illumination was removed by background correction.<sup>39</sup>

**Antibody–Antigen Affinity Measurements.** A model bioassay was performed using a plasmonic crystal by immobilizing antgoat IgG (antibody) on the surface of a crystal and measuring changes in normal incidence transmission at all wavelengths as solutions of increasing concentration of goat IgG (antigen) were injected into the flow cell containing the crystal. The surface of a crystal was prepared for biosensing by functionalizing the crystal with a carboxyl-terminated SAM by immersing the crystal in a 33 mM ethanolic solution of DTBA for 12 h. The crystal was thoroughly rinsed with ethanol and placed in a flow cell, and the terminal carboxyl groups of the SAM were activated using a 4:1 solution of EDC (200 mM)/NHS (50 mM) for 30 min. The crystal was then rinsed with PBS and exposed to a 0.5 mg/mL solution of protein G in PBS for  $\sim 30$  min. The crystal was subsequently rinsed with PBS, and a 0.05 mg/mL solution of antgoat IgG was injected into the flow cell for  $\sim 1.5$  h, followed by a buffer rinse. The extent of surface functionalization and specificity of the surface chemistry was tested by injecting a 0.01 mg/mL solution of bovine serum albumin (BSA). No change in transmission was observed upon injection of the BSA solution, indicating that the surface was blocked against nonspecific adsorption. The target molecule, goat IgG, was then injected at increasing concentrations, and the response was recorded as a function of time.

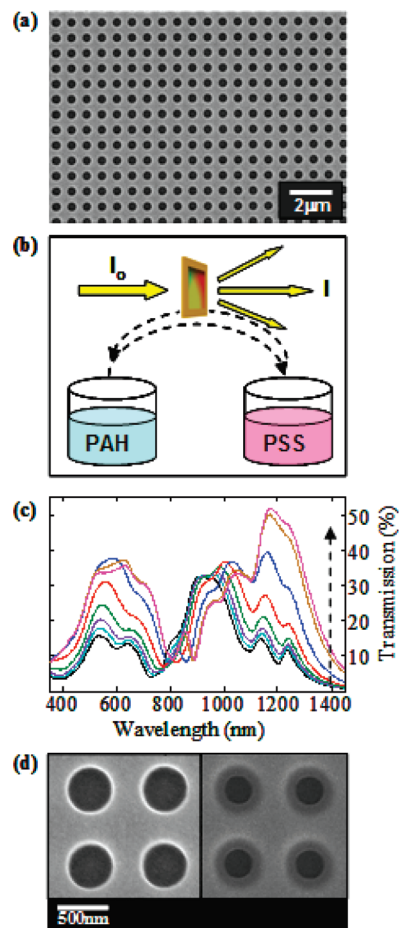


**Figure 1.** Layer-by-layer (LbL) assembly of polyelectrolytes on plasmonic crystals. (a) Scanning electron micrograph (SEM) of a 3D plasmonic crystal. (b) A schematic diagram illustrating the normal incidence transmission configuration used to probe the spectral response of the crystals during the LbL assembly of poly(allylamine hydrochloride) (PAH) and poly(sodium 4-styrenesulfonate) (PSS) multilayers on the surface of the crystals. (c) Transmission spectra of a crystal in air as a function of the PAH/PSS multilayer thickness, 0 nm (black); 5 nm (cyan); 15 nm (violet); 26 nm (green); 43 nm (red); 72 nm (blue); 92 nm (brown); and 99 nm (magenta). The dashed arrow indicates an increase in transmission with thickness at low frequencies. (d) High-magnification SEMs that show a crystal before (left) and after (right) LbL assembly of an  $\sim 99$  nm thick polyelectrolyte film.

## RESULTS AND DISCUSSION

Figure 1a shows a scanning electron micrograph of a plasmonic crystal consisting of a square array of cylindrical nanowells with diameters, depths, and periodicities of  $\sim 472$ , 350, and 728 nm, respectively. A continuous gold film was formed on the embossed polymer by sputter deposition, and the thickness of the gold on the top surface of the crystal and on the sidewalls and bottoms of the nanowells was  $\sim 35$ , 12, and 20 nm, respectively (Figure S2 in Supporting Information).<sup>40</sup> A carboxyl terminated SAM was formed on the surface of the crystal by placing it in an ethanolic solution of DTBA for 24 h. This SAM provided the surface charge required for electrostatic adsorption of the polycation, PAH, to the surface of the crystal. Additional polyelectrolyte layers were formed on the crystal by sequentially dipping the sample in PSS (polyanion) and PAH solutions using a previously reported LbL assembly protocol to form PAH/PSS multilayers.<sup>48</sup>

(59) Norland Products. 2008.

(60) Cunningham, B.; Lin, B.; Qiu, J.; Li, P.; Pepper, J.; Hugh, B. *Sens. Actuators, B* **2002**, *85*, 219–226.

(61) Gao, C.; Moya, S.; Lichtenfeld, H.; Casoli, A.; Fiedler, H.; Donath, E.; Mohwald, H. *Macromol. Mater. Eng.* **2001**, *286*, 355–361.

(62) Monahan, J.; Gewirth, A. A.; Nuzzo, R. G. *Anal. Chem.* **2001**, *73*, 3193–3197.

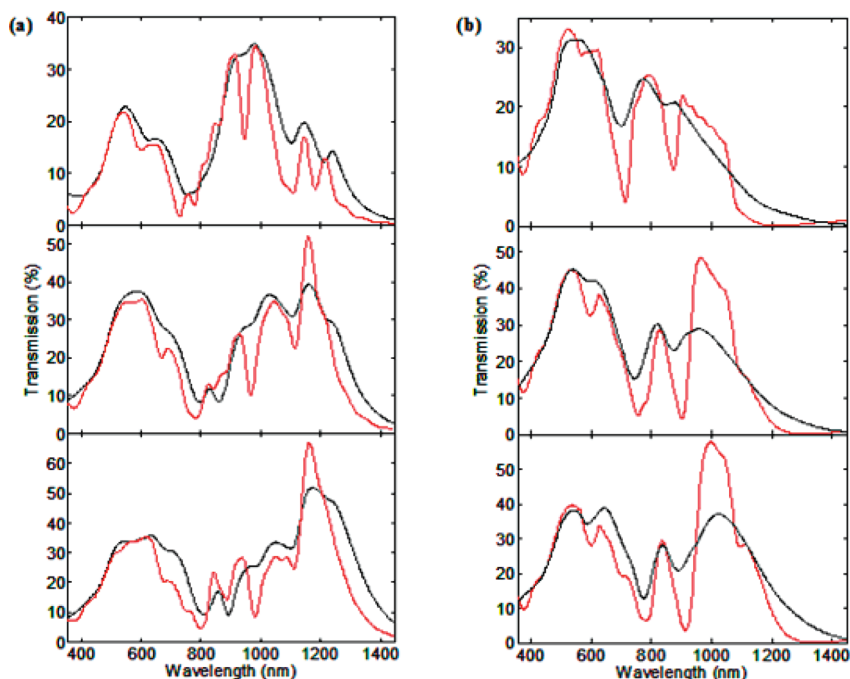


**Figure 2.** Experimental (black) and calculated (red) normal incidence transmission spectra of 3D plasmonic crystals with different design rules and polyelectrolyte layer thicknesses. (a) Plasmonic crystal with nanowell diameters, depths, and periodicities of 472, 350, and 728 nm, respectively, with polyelectrolyte layer thicknesses of 20 (top panel), 72 (middle panel), and 99 nm (bottom panel). (b) Plasmonic crystal with nanowell diameters, depths, and periodicities of 252, 350, and 564 nm, respectively, with the same polyelectrolyte thicknesses.

A schematic depiction of the process used to assemble the polyelectrolyte layers and characterize the spectral response of the plasmonic crystal to increasing film thickness is shown in Figure 1b. Figure 1c shows a series of normal incidence transmission spectra of the crystal collected in air during the LbL assembly process at increasing film thicknesses. The features in the spectra generally tend to redshift, broaden, and increase in intensity as the thickness of the multilayer film increases at the surface of the crystal. Figure 1d shows SEM images of the plasmonic crystal before and after the formation of polyelectrolyte multilayers. The thickness of the polyelectrolyte film measured in the SEM image near the edge of the nanowell ( $\sim 99$  nm) agrees with the thickness of the film formed on a flat gold film (control sample) measured by ellipsometry, which indicates good correlation between the polyelectrolyte film thickness measured on the flat gold slides and the film thickness on the surface of the plasmonic crystals. These results correlate well with those of previous studies that examined the LbL assembly of polyelectrolyte films on nanoporous templates including track-etched membranes or anodized aluminum oxide templates and found excellent fidelity in the layers and polymer tubes obtained. The latter template materials have nanopore diameters of 200–800 nm and aspect ratios (pore depth to pore diameter) of 25–300, challenging feature dimensions that exceed the relatively shallow nanowells of the plasmonic crystals examined in this work (aspect ratios of  $\sim 0.7$ ).<sup>45,63,64</sup>

Previously we demonstrated that full 3D FDTD calculations with appropriate periodic boundary conditions could be used to model the normal incidence transmission spectra and electromagnetic field distributions at the surface of 3D plasmonic crystals

with nanowell diameters, depths, and periodicities of 456, 350, and 748 nm, respectively.<sup>40</sup> The features in the spectra were assigned to thin film transmission of gold around 500 nm and various BW-SPPs, LSPRs, and WAs (or combinations thereof) at higher wavelengths. Here we use full 3D FDTD calculations to model the normal incidence transmission spectra of 3D plasmonic crystals with different design rules (diameters and periodicities) and polyelectrolyte film thicknesses (Figure 2). Figure 2a shows experimental (black) and calculated (red) normal incidence transmission spectra of a crystal with nanowell diameters, depths, and periodicities of 472, 350, and 728 nm, respectively, with total polyelectrolyte layer thicknesses of 20, 72, and 99 nm. Figure 2b shows experimental (black) and modeled (red) spectra of a crystal with nanowell diameters, depths, and periodicities of 252, 350, and 564 nm, respectively, for the same polyelectrolyte film thicknesses. For simplicity, the crystal geometries in parts a and b of Figure 2 will be referred to as the 728 and 564 nm periodicity crystals, respectively. As expected, the features in the spectra of the 564 nm periodicity crystal are blue-shifted with respect to the 728 nm periodicity crystal.<sup>65,66</sup> These data also show that the FDTD calculations capture the experimentally observed changes in the spectra quite well. For example, the FDTD spectra account for the experimentally observed increase and subsequent decrease in intensity of the features near 550 nm for both crystals when the polyelectrolyte film thickness is increased from 20 to 72 nm and from 72 to 99 nm, respectively.

(65) Shuford, K. L.; Gray, S. K.; Ratner, M. A.; Schatz, G. C. *Chem. Phys. Lett.* **2007**, *435*, 123–126.

(66) van der Molen, K. L.; Segerink, F. B.; van Hulst, N. F.; Kuipers, L. *Appl. Phys. Lett.* **2004**, *85*, 4316–4318.

(67) Rindzevicius, T.; Alaverdyan, Y.; Kall, M.; Murray, W. A.; Barnes, W. L. *J. Phys. Chem. C* **2007**, *111*, 11806–11810.

(63) Lee, D.; Nolte, A. J.; Kunz, A. L.; Rubner, M. F.; Cohen, R. E. **2006**, *128*, 8521–8529.

(64) Hou, S.; Wang, J.; Martin, C. R. *Nano Lett.* **2005**, *5*, 231–234.

To understand the spectral shifts described above (Figure 2) in greater detail requires extensive analysis of the FDTD calculated electromagnetic fields, which is beyond the scope of this text. Nonetheless we can comment on several general aspects. As described in ref 44, the transmission features can be related to broad LSPRs with fine structures due to BW-SPPs. In many cases we can assign local transmission minima to specific BW-SPPs at the gold–polyelectrolyte film interface and the gold–NOA interface. The similarity of the dielectric constants of the polyelectrolyte film and NOA (2.2 and 2.4, respectively) suggests the possibility of doublet structures, and several of these doublets are indeed observed in Figure 2.

The strength of our plasmonic crystals is the additional responsive complexity present in these optics relative to simpler SPR systems; however, this makes truly quantitative modeling of these structures difficult to achieve. In addition, we have previously shown that transmission features, particularly the relative intensities of these features, can be quite sensitive to the nanoscale structure of the gold at the surface of the crystals compared to the more ideal metal geometries assumed in calculations and that more fully quantitative modeling can be achieved by performing detailed, high-resolution electron microscopy studies of the structure of the gold at the surface of the crystals.<sup>32,40</sup> Here we show agreement in the positions of the spectral features in the experimental and calculated spectra and fairly good agreement in the intensities of the transmission features at many wavelengths and polyelectrolyte film thicknesses without the need for a highly detailed analysis of the nanoscale gold geometry at the surface of the crystal. This level of agreement is sufficient to identify the nature and contributions of the excitations to the spectral response as described above; however, it is not at a level to substitute calibration of the optics for quantitative sensing, which we perform using LbL assembly of polyelectrolyte thin films and self-assembled monolayers as described below.

The measured multispectral sensitivities of the 728 and 564 nm periodicity plasmonic crystals in Figure 2 to increasing polyelectrolyte layer film thicknesses are shown in parts a and b of Figure 3, respectively. Normal incidence transmission spectra of the crystals were collected in air after polyelectrolyte layers with known thicknesses were formed on the surface of the crystals using the LbL assembly protocol described above. Spectra were collected over the spectral range accessible by most inexpensive silicon-based detectors (350–1050 nm). The series of spectra were then referenced to and normalized by the initial spectrum of the crystal in air with no polyelectrolyte layers to generate the difference maps shown in the top panels of Figure 3a,b. This analysis is described by the following equation:

$$R_{\text{th}}(\lambda) = \frac{T_{\text{th}}(\lambda) - T_0(\lambda)}{T_0(\lambda)} \quad (1)$$

where  $R_{\text{th}}(\lambda)$  is the normalized optical response (i.e., normalized change in transmission) of the crystal as a function of wavelength for a specific polyelectrolyte layer thickness (th),  $T_{\text{th}}(\lambda)$  is the transmission of the crystal as a function of wavelength for a given polyelectrolyte layer thickness, and  $T_0(\lambda)$  is the initial transmission of the crystal as a function of wavelength with no polyelectrolyte layers. These maps show changes in transmission due to shifts in the positions and

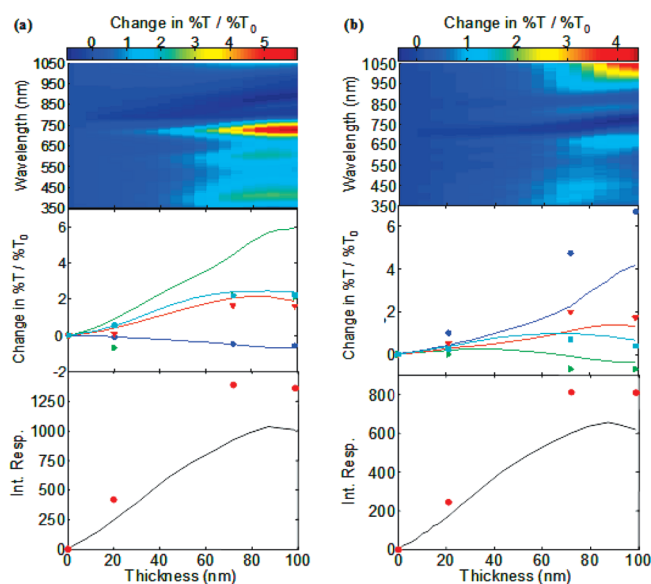


**Figure 3.** Difference maps and integrated responses (350–1050 nm) of plasmonic crystals with different design rules to increasing thickness of polyelectrolyte multilayers, measured in air at 20 selected film thicknesses. (a) The results of a crystal with a nanowell periodicity of 728 nm; and (b) the results of a crystal with a nanowell periodicity of 564 nm (same crystals described in Figure 2). The top panels present measured difference maps, the middle panels show the measured (curves) and calculated (overlaid symbols)  $R_{\text{th}}$  or changes in  $\%T/\%T_0$  as a function of the multilayer thickness at several wavelengths, and the bottom panels show the measured (black curve) and calculated (red circles) integrated multispectral responses (Int. Resp.). The single wavelengths shown in the middle panel of part a correspond to 408 (cyan squares), 607 (red triangles), 728 (green triangles), and 891 nm (blue circles), and those in the middle panel of part b correspond to 439 (cyan squares), 667 (red triangles), 768 (green triangles), and 1044 nm (blue circles). The last two green triangles in the middle panel of part a corresponding to the calculated  $R_{\text{th}}$  for the  $\sim 72$  and 98 nm thick polyelectrolyte film overlap with the cyan squares.

intensities of the features in the spectrum as the thickness of the polyelectrolyte layer is increased. In contrast to our previous work,<sup>24</sup> here we normalize the change in  $T$  by  $T_0$  to compensate for the effects of Fresnel reflections on the measured optical response and capture only the sensing signal associated with the plasmonic resonances and WAs (Figures S3 and S4 in the Supporting Information).

The middle panels of parts a and b of Figure 3 show the experimental (curves) and FDTD calculated (symbols) normalized changes in transmission as a function of polyelectrolyte film thickness at selected wavelengths. These results illustrate the strong wavelength and distance dependent surface sensitivities of the crystals, where the sensitivity, given by the slope of the curve, can increase or decrease as the thickness of the polyelectrolyte layer is increased. Although these crystals clearly exhibit different and complex wavelength dependent optical responses as a function of the polyelectrolyte film thickness (Figure 3a,b, top and middle panels), the crystals yield qualitatively similar integrated multispectral responses (Figure 3a,b, bottom panels), which is calculated over the measured wavelength range (350–1050 nm) using the following equation:

$$\text{IR} = \int_{350\text{nm}}^{1050\text{nm}} |R_{\text{th}}(\lambda)| d\lambda \quad (2)$$

where IR is the integrated response and  $R_{\text{th}}(\lambda)$  is given by eq 1. The crystals exhibit an increase in IR to increasing polyelectrolyte film thicknesses until a thickness of  $\sim 90$  nm, after which the IR decreases with increasing film thickness. The linear correlation between film thickness and IR over thicknesses greater than the size of typical protein and diagnostic biomarkers makes these platforms suitable for performing quantitative bioassays as will be demonstrated below. A qualitatively similar distance-dependent response was observed by Rindzevicius et al.<sup>67</sup> when measuring the LSPR peak shift of short-range ordered gold nanodisks and nanoholes upon the formation of Langmuir–Blodgett multilayers.

While we have shown that the FDTD calculations capture reasonably well the experimentally measured spectral features (Figure 2) and changes in transmission caused by thin film assembly (middle panels of Figure 3a,b), some discrepancies are observed in the latter calculations at specific wavelengths. The middle panel of Figure 3a shows that at large film thicknesses the calculated  $R_{\text{th}}$  at  $\lambda = 728$  nm (green triangles) deviate from the measured  $R_{\text{th}}$  (green curve) and overlap with the calculated  $R_{\text{th}}$  at  $\lambda = 408$  nm (cyan squares). Discrepancies of this sort can occur when spectral features shift slightly differently or have different widths in theory and experiment.

The sensitivity of the crystals to surface binding events is determined by taking the derivative of the IR versus film thickness curves in the bottom panels of Figure 3a,b. These plots clearly show that the 728 nm periodicity crystal is more sensitive to surface binding events than the 564 nm periodicity crystal. Fitting the approximately linear region of the curves over film thicknesses of  $\sim 0$ – $80$  nm yields thin film sensitivities of the integrated response (IR) of  $\sim 13$  and  $9$  IR/nm for the 728 and 564 nm periodicity crystals, respectively. These thin film sensitivities describe the change in IR measured across the visible spectrum per nanometer of polyelectrolyte film (i.e., a film thickness) formed on the surface of the crystal and cannot be directly compared to the more traditional bulk refractive index sensitivity values reported in the literature for SPR sensors that describe the change in the SPR position or intensity at a single wavelength per unit increase in the bulk refractive index of a solution in contact with the sensor.<sup>36,68</sup> Multispectral analysis of a bulk refractive index sensitivity calibration experiment is provided in the Supporting Information for the interested reader (Figure S5 and associated text). The nondimensionless, multispectral bulk refractive index sensitivity of a  $\sim 730$  nm periodicity crystal with a 35 nm nominal gold thickness is  $\sim 41\,000$  (% $T$ ) nm/RIU. As the units suggest, the multispectral analysis approach weights both change in the positions and intensities of the many spectral features over the multiple responsive wavelengths of a plasmonic crystal and is not a measure of the change in position or intensity of a single resonance or wavelength as is commonly used to describe the sensitivity of SPR sensors.<sup>36,68</sup>

The effect of gold thickness on the sensitivity of these optics to surface binding events was also investigated. We found that the sensitivity increased with gold thickness up to a maximum around  $\sim 120$  nm, after which the sensitivity decreased (Figure

S6 in the Supporting Information). These surface sensitivity results are in good agreement with experimentally determined and modeled bulk RI sensitivities of the crystals as a function of gold thickness.<sup>69</sup>

Previously we showed that a simple mathematical model developed for quantifying binding events using planar gold film SPR spectroscopy can be applied to quantitatively interpret the real-time response of plasmonic crystals to binding events in solution.<sup>32</sup> This adapted model relates a measured IR to an effective film thickness ( $d$ ) adsorbed to the surface of a crystal by the following equation:<sup>36</sup>

$$\text{IR} = m(n_a - n_s)[1 - \exp(-2d/l_d)] \quad (3)$$

where  $l_d$  is the decay length of the electric field at the surface of the crystal, which is  $\sim 25\%$ – $50\%$  of the wavelength of the incident light,  $m$  is the bulk RI sensitivity, and  $n_a$  and  $n_s$  are the refractive indices of the thin film adsorbed to the surface of the crystal (e.g., protein) and the bulk dielectric above the thin film (e.g., buffer), respectively. This model assumes a uniform characteristic  $l_d$  of the plasmon evanescent field into the dielectric medium above a planar gold film. This assumption is valid for a planar dielectric–gold interface with a single SPP resonance peak but is an oversimplification for our plasmonic crystals that support multiple plasmonic modes (LSPRs and SPPs) with characteristic decay lengths and WAs and exhibit changes in both peak positions and intensities over most of the spectral range with changes in RI.<sup>36</sup>

Given the complexity of the optical response of the crystals, a more direct approach to quantify binding events at the surface of the crystals is to calibrate the optical response of the sensors by measuring a molecular layer of known thickness. Here, we show that the short-range linearity (within  $<70$  nm of the crystal surface) of the IR of the plasmonic crystals to thin film assemblies can be used together with molecular rulers, molecular assemblies with known thicknesses such as SAMs of alkanethiols on gold, to calibrate these optics to effect quantitative imaging and speciation of surface binding events. This approach directly takes into account the heterogeneous fields of the SPPs and LSPRs at the surface of the crystal and contributions from WAs that are not accounted for in eq 3. It also eliminates the need to estimate the decay length of the fields at the surface of the crystals and the need to measure bulk RI sensitivity factors by directly measuring a surface specific sensitivity factor.

As a demonstration, three proteins with different molecular weights were patterned via nonspecific adsorption on the surface of a crystal using a microfluidic device (Figure 4a) and imaged using an optical microscope equipped with a CCD camera and an unfiltered white light source (i.e., a halogen bulb) (Figure 4b). The three proteins, patterned from left to right in the image, were fibrinogen (MW  $\sim 340$  kDa),  $\gamma$ -globulins (MW  $\sim 160$  kDa), and myoglobin (MW  $\sim 14.4$  kDa). The protein lines are clearly visible due to the refractive index difference between the protein patterned and unpatterned regions. The image contrast (defined as the intensity of the protein patterned areas minus the intensity of the unpatterned areas) was converted to thickness using a calibration factor that was

(68) Shumaker-Parry, J. S.; Campbell, C. T. *Anal. Chem.* **2004**, *76*, 907–917.

(69) Maria, J.; Truong, T. T.; Yao, J.; Lee, T.-W.; Nuzzo, R. G.; Leyffer, S.; Gray, S. K.; Rogers, J. A. *J. Phys. Chem. C* **2009**, *113*, 10493–10499.

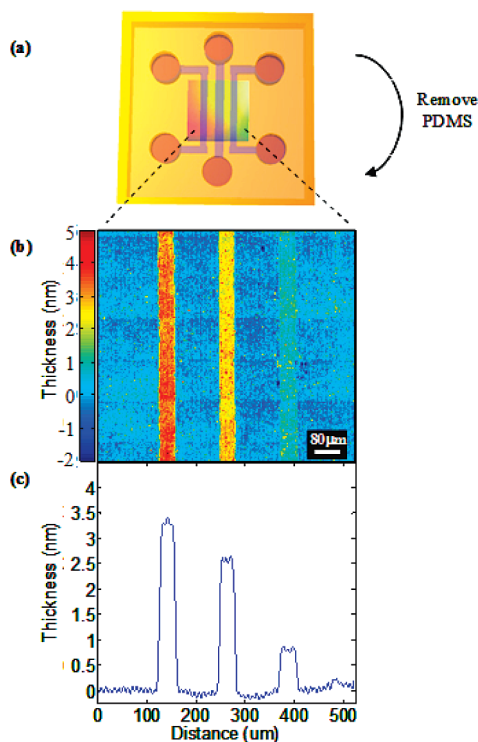


**Figure 4.** Quantitative spatial imaging of nonspecifically adsorbed proteins to the surface of a plasmonic crystal. (a) A schematic illustrating the use of a three channel PDMS microfluidic device to pattern the surface of a crystal. (b) Transmitted light image of three lines of nonspecifically adsorbed proteins on the surface of a crystal. The proteins from left to right are fibrinogen (MW = 340 kDa),  $\gamma$ -globulins (MW = 160 kDa), and myoglobin (MW = 14.4 kDa). (c) The average line profile through the image in panel b.

previously determined by measuring the image contrast upon the formation of an  $\sim 2$  nm thick SAM (a change in image intensity of  $\sim 0.04 (\pm 0.01)$ ). Figure 4c shows the average line profile of the image shown in Figure 4b. As expected, the intensity of the protein lines scaled with their molecular weight and the estimated thickness of each protein agreed well with the ellipsometrically measured thickness of the protein on a planar gold film.<sup>70</sup> The important aspects of this demonstration include (i) spatially resolved imaging of molecular adsorbates can be achieved with these crystals using a common laboratory microscope equipped with a CCD camera and a white light source; (ii) image intensity changes scale with the molecular weight of the adsorbate; and (iii) quantitative analysis of the imaging can be achieved by calibrating the response of the crystal with a molecular ruler. The signal-to-noise level of the image shown is not intrinsic to the plasmonic crystal optic and can be optimized by changing acquisition parameters such as increasing frame averaging.

A more relevant system to study in regards to bioassays is the *in situ* thin film surface sensitivity of a plasmonic crystal in water to increasing polyelectrolyte film thickness (Figure 5). The middle panel of Figure 5 shows that a 728 nm periodicity crystal in water exhibits complex wavelength and distance-dependent surface sensitivity to binding events, similar to the response observed for a 728 nm periodicity crystal in air. Unlike the IR response of the crystal in air, however, the IR of the crystal in water saturates rather than decreases in magnitude at film thicknesses  $>95$  nm (Figure 5, bottom panel). An important point to note is that the single wavelength responses

(70) Mack, N. H.; Dong, R.; Nuzzo, R. G. *J. Am. Chem. Soc.* **2006**, *128*, 7871–7881.

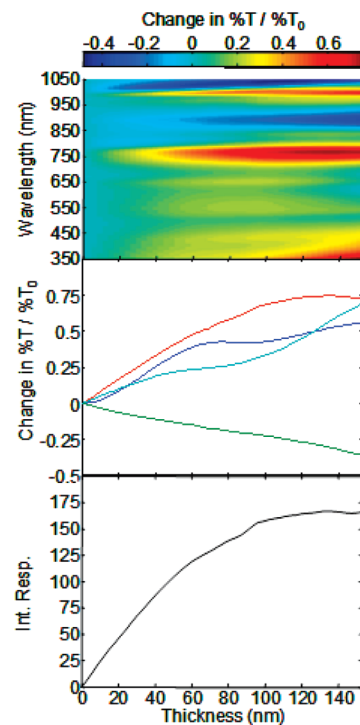


**Figure 5.** Difference map and integrated response (355–1050 nm) of a crystal with a periodicity of 728 nm to increasing thickness of a polyelectrolyte multilayer, measured in water at 52 selected film thicknesses. The top panel presents the difference map, the middle panel shows the  $R_{th}$  or change in  $\%T/\%T_0$  as a function of the multilayer thickness at several wavelengths: 357 (cyan), 769 (red), 894 (green), and 996 nm (blue). The bottom panel shows the corresponding integrated multispectral response (Int. Resp.).

of the crystal in water remain sensitive to surface binding events at thicknesses  $>95$  nm, which makes single wavelength measurements more useful for analyzing thick films. The IR, however, is still a useful metric for the detection of binding events over distances that are relevant for most bioassays and provides greater signal-to-noise than single wavelength measurements, as described previously.<sup>32</sup>

The binding of solution-phase goat IgG to surface immobilized antigoat IgG was chosen as a model system for demonstrating the utility of full 3D plasmonic crystals for performing quantitative analysis of biomolecular interactions relevant to diagnostic bioassays. To this end, the surface of a crystal was prepared for selective detection of solution-phase goat IgG using a multistep surface functionalization protocol. First, protein G was covalently coupled to the surface of a crystal using carboxyl-terminated SAMs and EDC/NHS succinimidyl ester chemistry.<sup>71,72</sup> The protein G served as a receptor to immobilize and orient antigoat IgG on the surface of the crystal such that the antigen-binding fragment of the antibody was oriented away from the surface so that it could capture the solution-phase antigen, goat IgG. BSA was then injected into the flow cell and no response was observed, which indicated that the crystal surface was blocked against nonspecific binding. Equilibrium analysis of the antigoat IgG/goat IgG pair was probed by increasing the concentration of goat IgG in the running buffer as a step gradient from 1 pM to 1  $\mu$ M. Each concentration of goat IgG was incubated in the flow cell for  $\sim 1$  h before injection of the next goat IgG solution.

(71) Cao, H.; Xu, S.-Y. *J. Mater. Sci.* **2008**, *19*, 567–575.

(72) Tengvall, P.; Jansson, E.; Askendal, A.; Thomsen, P.; Gretzer, C. *Colloids Surf., B* **2003**, *28*, 261–272.

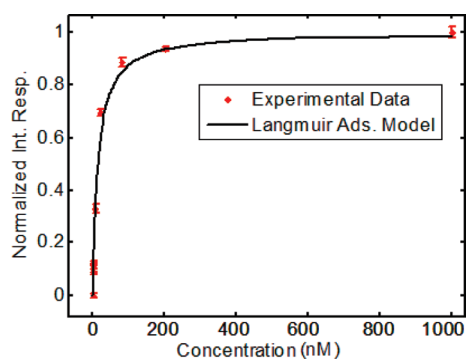


**Figure 6.** Quantitative response curve for the binding of solution-phase goat IgG to surface immobilized anti-goat IgG. The plot shows the normalized integrated response of a crystal with a periodicity of  $\sim 740$  nm to increasing concentrations of goat IgG (red data points). Nonlinear regression of the binding curve (black line) yielded a surface confined affinity constant of  $\sim 7 \times 10^7 \text{ M}^{-1}$ .

Incubation times for immunoassays depend on several factors including the concentrations of the binding pairs, the ionic strength of the solution, and the affinity constant of the binding pair.<sup>73,74</sup> The 1 h incubation time was selected to maximize the equilibrium binding response for several of the lower antibody concentrations measured in this work.

The binding profile of the antibody–antigen pair is shown in Figure 6. This plot shows the estimated surface coverage ( $\theta$  = normalized IR) of the crystal as a function of the solution-phase goat IgG concentration and exhibits a commonly observed adsorption isotherm profile.<sup>75–77</sup> The binding constant of the antibody–antigen pair was estimated by fitting the binding profile to a Langmuir isotherm:<sup>75,77</sup>

$$\theta = \frac{K_a[\text{IgG}]}{1 + K_a[\text{IgG}]} \quad (4)$$

where  $K_a$  is the apparent affinity constant and  $[\text{IgG}]$  is the solution-phase goat IgG concentration. The best fit to the data yielded an estimated surface confined affinity constant of  $\sim 7 \times 10^7 \text{ M}^{-1}$ , which is consistent with affinity constants reported in the literature for IgG/anti-IgG binding pairs.<sup>75,77</sup> These results demonstrate that the crystals and multispectral analysis protocol can be used to quantitatively measure the equilibrium binding constant of a binding pair (i.e., the IR response for a given analyte concentration is directly related to the equilibrium binding affinity constant).

A commonly used figure of merit of a sensor is the limit of detection (LOD), which is related to the resolution of the system (the smallest detectable refractive index change). The resolution of a plasmonic sensing platform is determined by intrinsic (e.g., the refractive index sensitivity of the device itself) and extrinsic (e.g., signal averaging, thermodynamic affinity constant of the binding pair, molecular weight of analyte, surface chemistry (ligand density, nonspecific binding, signal amplification), temperature fluctuations,

and noise associated with the spectrometer, optics, source, and detector) factors. Our experiments were performed without signal averaging, temperature control, or chemical amplification. The extrinsic limitations inherent in the detection system restricted our current LOD for these *in situ* measurements to antibody binding coverages that would produce an integrated response of  $\sim 0.3$  (or roughly  $3\times$  the limiting noise level of a blank sample). Stated differently, this sensor without further optimization and absent other complications will discriminate coverage as low as  $\sim 3\%$  of a monolayer of the conjugate antibody, which for an unamplified equilibrium assay corresponds to a solution concentration of  $\sim 400 \text{ pM}$  (or equivalently a surface coverage of  $\sim 16 \text{ ng/cm}^2$ ). For comparison, studies using prism coupled SPR sensors have reported achievable limits of detection for antibody binding at surface coverages of  $\sim 0.3 \text{ ng/cm}^2$ .<sup>78</sup> As noted above, the detection limits depend on the affinity constants of the specific binding partners and the quality of the surface chemistry used in the assay. It therefore is instructive to consider comparisons based on the adsorption of a similar protein, bovine serum albumin (BSA), adsorbed on gold. The reported nonoptimized LOD of the plasmonic crystal in this case differs by about a factor of 2 from the LOD reported for a prism-coupled SPR.<sup>32,68</sup>

While it is possible to improve our LOD by employing temperature control, signal averaging using a spectrometer equipped with a photodiode array, and signal amplification strategies, it remains that real LODs will likely be limited in unamplified assays by features other than the instrument given the magnitude of the equilibrium binding affinity of the immunoassay pairing. Foremost among these for a real titer would be the obscuring background provided by nonspecific adsorption of molecules in the complex matrix. The present data therefore suggest that a considerable opportunity for improving the capabilities of plasmonic label-free detection systems in fact resides in the chemistries used to enable them.

## CONCLUSIONS

This work described the use of the LbL assembly of polyelectrolytes to systematically study the thin film sensitivity of full 3D plasmonic crystals in air and liquid environments. The effects of gold thickness and design rules (nanowell diameter and periodicity) on the thin film sensitivity of the crystals were investigated, and full 3D finite-difference time-domain calculations were used to quantitatively model and elucidate the experimentally observed thin film sensitivities. It was found that crystals with gold thicknesses of  $\sim 120 \text{ nm}$  are more sensitive to surface binding events than crystals with either thinner or thicker gold films. The linearity of the integrated multispectral response of the crystals to a thin film assembly ( $< 70 \text{ nm}$ ) allowed the use of a molecular ruler of known thickness, a SAM, to calibrate these optics for quantitative spatial imaging and speciation of surface-adsorbed proteins. The functionality of these devices for quantitative biosensing was further demonstrated by measuring the affinity constant of an antibody/antigen binding pair. These results together with the low-cost of fabrication, simple readout apparatus and geometry, compact form factors, and potential for direct integra-

(73) Quinley, E. D. *Immunohematology: Principles and Practice*, 2nd ed.; Lippincott Williams & Wilkins: Philadelphia, PA, 1998.

(74) Law, B., Ed. *Immunoassays: A Practical Guide*, 1st ed.; Taylor & Francis: Bristol, PA, 1996.

(75) Riboh, J. C.; Haes, A. J.; McFarland, A. D.; Yonzon, C. R.; Van Duyne, R. P. *J. Phys. Chem. B* **2003**, *107*, 1772–1780.

(76) Masson, J.-F.; Battaglia, T. M.; Khairallah, P.; Beaudoin, S.; Booksh, K. S. *Anal. Chem.* **2007**, *79*, 612–619.

(77) Yu, C.; Irudayaraj, J. *Biophys. J.* **2007**, *93*, 3684–3692.

(78) Campbell, C. T.; Kim, G. *Biomaterials* **2007**, *28*, 2380–2392.

tion into microfluidic networks make these devices simple to implement and interesting candidates for label-free array based detection.

#### **ACKNOWLEDGMENT**

M.E.S. and J.Y. contributed equally to this work. The authors acknowledge the support of the U.S. Department of Energy (Grant DEFG02-91-ER45439). This work was carried out in part in the Frederick Seitz Materials Research Laboratory Central Facilities, University of Illinois, which are partially supported by the U.S. Department of Energy under Grants DE-FG02-07ER46453 and DE-FG02-07ER46471. The work at Argonne National Laboratory was

supported by the U.S. Department of Energy, Office of Science, Office of Basic Energy Sciences, under Contract No. DE-AC02-06CH11357. We also thank Christopher R. Anderton for assisting with the layer by layer assembly and taking spectral measurements.

#### **SUPPORTING INFORMATION AVAILABLE**

Additional information as noted in text. This material is available free of charge via the Internet at <http://pubs.acs.org>.

Received for review April 16, 2009. Accepted June 30, 2009.

AC900819J